Diurnal Variation of Desert Midwave Infrared Images

Kim T. Constantikes, Michael E. Thomas, and Emily D. Claussen

A specialized camera system was constructed and used to record very large field-of-view images of a southwestern U.S. desert during January 1996. Images were recorded approximately every 6 min continuously for up to 48 h. We postprocessed the images and performed some radiometric analysis and model comparisons. Several observed phenomena are noteworthy, including the following: desert foliage reflectance of the Sun is significant in the midwave and causes apparent temperatures above ambient, and an as yet unexplained low-apparent-temperature "notch" in elevation radiance profiles occurs only just after sunrise.

INTRODUCTION

We performed an infrared survey of a desert area from 11 January to 15 January 1996. This survey was done with a specialized camera system designed and fabricated by the APL Fleet Systems Department's Electro-Optical Systems Group. The distributed camera instrument system consisted of a 24 × 24 × 36 in. instrument pallet mounted on the top of a 100-ft tower and a control and analysis station at the bottom of the tower.

The instrument pallet included a Cincinnati Electronics focal plane array camera with digital and analog interfaces configured for 1-mrad pixel size on an image size of 160 × 120 pixels, 0.053-μW/cm^2·sr·bit radiance resolution, 0.050-pW/cm^2 noise equivalent irradiance, and operation in a sub-band of the 3- to 5-μm waveband. This camera and a commercial 8-mm video camera were mounted on a DC servo-driven elevation-over-azimuth pointing head. Two calibration sources and a temperature and humidity probe were also mounted on the pallet. A local computer controlled the cameras and servos and collected image data.

The instrument pallet was connected to a ground control and analysis station via a local area network (10BaseT) and two video coaxial lines dropped from the top of the tower. The ground station computer managed an automated data collection task using WiT, a distributed signal and image processing package. Control and data collection were described as a signal flow graph in the visual editor of the package, and the instrument pallet computer was configured as a server node on the network. Thus, we had complete and flexible control of our instrument with few physical interconnections and could analyze the data at the time of collection.

Data collection was accomplished by precisely pointing the IR camera and collecting a mosaic 8 images wide by 6 images high (Fig. 1). The center of the mosaic points roughly north, and the center row is roughly the horizon. Although the accuracy of the servo system was much better than the camera pixel size (30 mrad for the servos versus about 1 mrad for the pixel), uncertainty in the camera focal length of about

K. T. CONSTANTIKES, M. E. THOMAS, AND E. D. CLAUSSEN
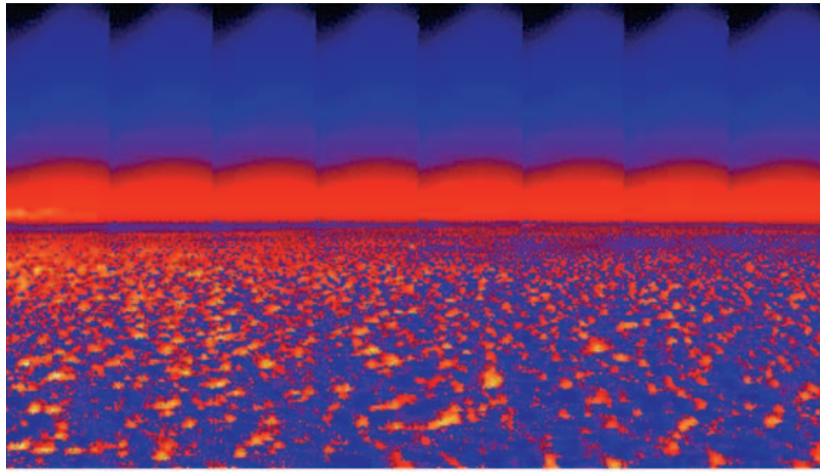
Figure 1. A mosaic image consisting of 48 separate images organized in an 8 × 6 matrix. The total field of view of the image is 68 × 51° and has 1-mrad spatial resolution, i.e., it is 1184 × 666 pixels. Images were taken at about 1500 Coordinated Universal Time (UTC) from a location N 032°24.422′, W 106°20.724′, and the image center points roughly north. Note the reflection from the mountains at the left of the image, and the implicitly non-Lambertian nature of the desert floor reflectance as indicated by strong solar reflection at the left of the image (reciprocal direction of the Sun). Note also the dark band separating the mountains from the desert floor. The bar below the image shows increasing radiance from left to right.

a result of a nonuniform blackbody used for camera nonuniformity correction. Figure 2 is an image taken at 1900 UTC, with the Sun near zenith. Spatial nonuniformity of response of the camera is not so apparent because of the larger dynamic range of the image. Although we have not removed nonuniformity at this date, it is a relatively straightforward procedure to estimate the nonuniformity from the images themselves and then correct the composites accordingly. The entire time series of images was used to create an animation in grayscale, pseudocolor, and edge-enhanced pseudocolor. These animations proved to be extremely valuable in the discovery of phenomena and conceptualization of the physics of the scene.

We also computed radiance profiles as a function of elevation angle by averaging together all columns of a composite image (shown later in Fig. 4). Further discussion of these profiles is deferred to the next section. Apparent temperatures were computed by inverting the Planck relationship on the relevant temperature and waveband intervals using a least-squares fit of a low-order logarithm polynomial. Basic descriptive statistics (mean, standard deviation, minimum, and maximum) were computed for each image and time and were used to construct time series composites of local (9 × 6 pixel) statistics. Figure 3 shows local statistics for 148 × 111 pixel neighborhoods.

5% and concerns about torsional and latitudinal flexures in the tower led us to overlap adjacent images slightly. Forty-eight images were collected and stored on the pallet computer, along with a visible video record, during each collection event. The collection event took about 1 min, after which the cameras would idle while the ground computer constructed the composite image and calculated basic statistics for the management of camera dynamic range and fault detection. This process continued for about 48 h, during which time the system was mostly unattended.
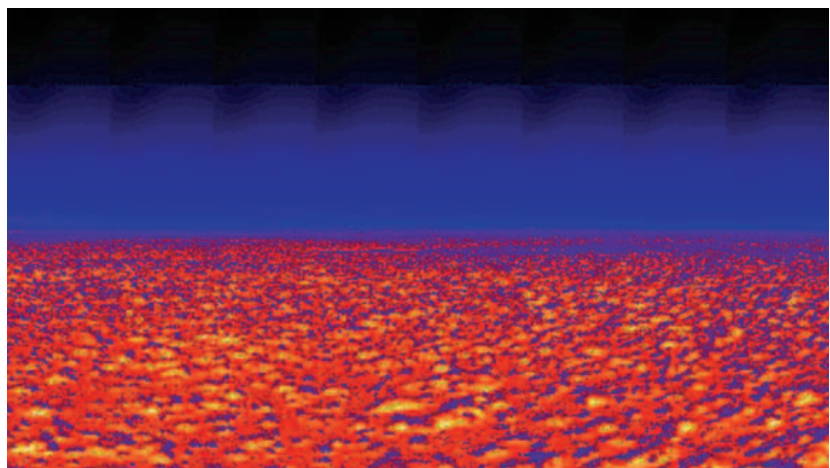
IMAGE POSTPROCESSING AND ANALYSIS

After we returned to APL, we used a correlation matching method to register overlapped regions of vertically and horizontally adjacent images. We found that the tower vibrations were not significant and that registration of images was constant over several hours. We determined the nonoverlapped portion of each image was 148 × 111 pixels; thus, the total field of view of a composite image was 68 × 51°. Figure 1 is a composite image collected at 1500 Coordinated Universal Time (UTC), or just after sunrise. Nonuniformity in the sky is

Figure 2. A composite with the same measurement conditions as Fig. 1 except taken at 1900 Coordinated Universal Time (UTC). The Sun is nearly behind the camera, so the desert reflectance is nearly uniform.
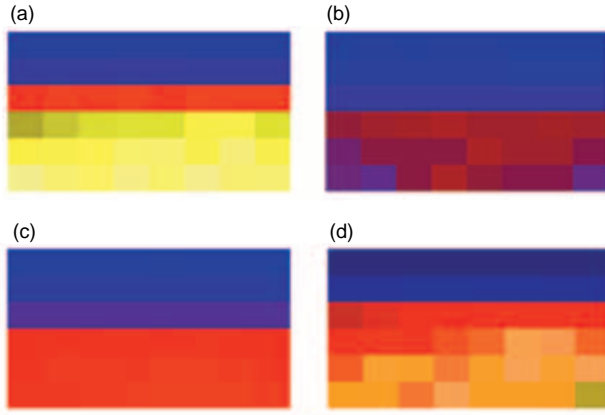
Figure 3. Local statistics of a composite image computed on 148 × 111 pixel neighborhoods. (a) Maximum radiance, (b) minimum radiance, (c) mean radiance, and (d) standard deviation of radiance. Images a, b, and c are on the same radiometric scale, whereas image d is 10 times the other scales. The spatially nonuniform desert radiance in images a, b, and c is indicative of non-Lambertian reflectance. Also, the decrease of standard deviation in the elevation direction occurs because the camera detector solid angle becomes larger than the radiance spatial correlation of the desert floor.

INTERPRETATION AND MODEL COMPARISONS

The infrared midband desert scenes have two distinct regions, sky radiance and Earth radiance. The sky radiance L_{sky} represents emission from the atmosphere and is driven by the air temperature. The Earth radiance is more complicated because it is composed of several components:[1] surface radiance $L_{surface}$, reflected sky radiance L_{refsky}, reflected solar radiance, L_{Sun}, and atmospheric path radiance L_{path}. The Earth radiance is largely driven by the variation in solar irradiance, in turn a function of solar elevation angle. Because of the long visibility range at the time of the measurements, we assumed that atmospheric scattered radiance was insignificant.

A sky radiance model for the 8- to 12-μm region, developed by Saunders,[2] is adapted for application to the 3- to 5-μm band. The following semi-empirical formula for sky radiance as a function of the zenith angle θ is proposed:

$$L_{sky}(\theta, T, T_{sky}, p_{H_2O}) = A(T) - B(T, T_{sky})$$
$$\times \exp[-C(p_{H_2O})(\sec\theta - 1)], \quad (1)$$

where $A(T)$ is the band-integrated blackbody radiance at the near-surface air temperature T, $B(T, T_{sky})$ is determined by requiring $A(T) - B(T, T_{sky})$ to be the vertical sky radiance, T_{sky} is the upper-altitude air

temperature, and $C(p_{H_2O})$ is the vertical optical depth from the observer to 5 km as a function of the water vapor partial pressure. In the model calculations, the surface air temperature is determined by computing the sky brightness temperature near the horizon. The surface air temperature varies throughout the day. The sky temperature represents the more thermally stable upper atmosphere and is therefore held constant. It is chosen to be T_{sky} = 256 K. The optical depth coefficient was determined to be 0.15 for a water vapor partial pressure of 0.37 kPa.

The surface radiance $L_{surface}$ is defined as follows:

$$L_{surface}(\delta, p_{H_2O}) = (1 - \text{TIR})A(T_{ground})$$
$$\times \tau_{path}(\delta, p_{H_2O}), \quad (2)$$

where TIR is the total integrated reflectance of the surface (dominated by vegetation), $A(T_{ground})$ is the band-integrated blackbody radiance at the ground temperature T_{ground}, and $\tau_{path}(\delta, p_{H_2O})$ is the band-averaged path transmittance from the surface location to the observer and depends on the look angle δ and the water vapor partial pressure. The ground temperature is kept constant and set to the minimum nighttime air temperature of 270.4 K. The TIR used in model calculations is 0.6. We assumed that the surface is Lambertian.

The reflected sky radiance L_{refsky} is defined as follows:

$$L_{refsky}(T, \delta, p_{H_2O}) = \text{TIR}\left[\int_0^{\frac{\pi}{2}} L_{sky}(\theta, T, p_{H_2O})\sin\theta\, d\theta\right] \quad (3)$$
$$\times \tau_{path}(\delta, p_{H_2O}).$$

As Eq. 3 shows, the reflected sky radiance depends on the low-altitude air temperature.

The reflected solar radiance L_{Sun} is defined as follows:

$$L_{Sun}(\theta_{Sun}, \delta, p_{H_2O}) = E_{Sun}(\theta_{Sun}, p_{H_2O})$$
$$\times \text{TIR}\,\tau_{path}(\delta, p_{H_2O}), \quad (4)$$

where $E_{Sun}(\theta_{Sun}, p_{H_2O})$ is the solar irradiance at the surface of the Earth and is given by

$$E_{Sun}(\theta_{Sun}, p_{H_2O}) = E_{Sun 0}\exp[-2.44C(p_{H_2O})\sec\theta_{Sun}],$$

where θ_{Sun} is the solar zenith angle, E_{Sun0} is the solar irradiance at the top of the atmosphere, and the exponential factor represents the transmittance from the observer to space.

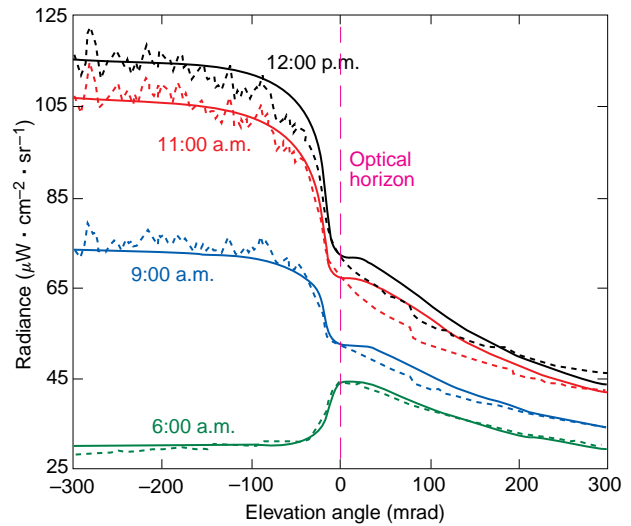The atmospheric path radiance L_{path} is defined as follows:

$$L_{path}(T, \delta, p_{H_2O}) = A(T)[1 - \tau_{path}(\delta, p_{H_2O})]. \quad (5)$$

Summing all the different radiances yields the observed radiance. A comparison of the experimental measurements over a 6-h period and the radiance model is shown in Fig. 4. The solar elevation angle was recorded and used in the computations for θ_{Sun}. The sky radiance model accurately predicts the measured sky radiance from 6:00 to 9:00 a.m. The agreement is not quite as good as noon approaches, suggesting more atmospheric layers are needed in the model. The radiance signature from the desert is composed of the path, ground, and reflected sky radiance at night and reflected solar radiance during the day. The model does account for the curvature of the Earth, but it does not include atmospheric refraction. For this reason, the optical horizon indicated in Fig. 4 is the geometrical horizon and does not change throughout the day in the model.

SUMMARY

We have measured large field-of-view images of the desert floor and horizon with high spatial resolution and for extended intervals. These data have been used for validation of models in work and for visualization of the diurnal variations of desert clutter. Additional measurements are planned on sky radiance and atmospheric attenuation and radiance. These measurements will be used to resolve the nature of the dark band observed at the horizon at sunrise only and to refine existing models.

Figure 4. Comparison between model (smooth curves) and experimental (dashed curves) radiance at four different times: 6:00 a.m. before sunrise and air temperature of 270.4 K, 9:00 a.m. solar elevation angle of 19° and air temperature of 275.4 K, 11:00 a.m. solar elevation angle of 34° and air temperature of 284.7 K, and 12:00 p.m. solar elevation angle of 36° and air temperature of 286.5 K.

REFERENCES

[1]Constantikes, K. T., "Modeling and Synthesizing Infrared Ocean Clutter," *Johns Hopkins APL Tech. Dig.* **16**(2), 171–186 (1995).
[2]Saunders, P. M., "Radiance of Sea and Sky in the Infrared Window 800–1200 cm^{-1}," *J. Opt. Soc. Am.* **49**, 645–652 (1968).

THE AUTHORS

KIM T. CONSTANTIKES is a Senior Staff engineer in APL's Fleet Systems Department. He received his B.S. degree in applied physics in 1983 from Ohio University. He then attended Carnegie Mellon University with a Benjamin Franklin Fellowship and received an M.S. degree in electrical and computer engineering in 1985. At Carnegie Mellon, he researched topics in pattern recognition and sensors in the Smart Sensors Laboratory of the Robotics Institute. Mr. Constantikes joined APL's Electro-Optical Systems Group in 1985, where he has worked on various computational and algorithmic aspects of imaging systems used for target acquisition, tracking, and recognition, as well as image-matching navigation. His current interests include image and scene modeling, image processing algorithms, target detection in clutter, and computer graphics. His e-mail address is Kim.Constantikes@jhuapl.edu.

MICHAEL E. THOMAS obtained a B.E.E. from the University of Dayton in 1973, and M.S. and Ph.D. degrees from Ohio State University in 1976 and 1979, respectively. Since joining APL in 1979, he has worked on electromagnetic propagation and optical properties of materials. In 1982, he was a postdoctoral fellow in the Department of Physics at the Naval Postgraduate School. In 1988, Dr. Thomas became a faculty member of the Part-Time Programs in Engineering and Applied Science at The Johns Hopkins University G.W.C. Whiting School of Engineering, teaching courses on optical propagation and lasers. His current research interests include experimental and theoretical modeling of atmospheric propagation in the infrared, DIAL lidar, optical and infrared window materials, and the infrared properties of high-pressure gases. He has published over 70 articles in books and journals. His e-mail address is Michael.Thomas@jhuapl.edu.

EMILY D. CLAUSSEN received a B.S. degree in electrical engineering from Purdue University in 1994. She has been an Associate Staff engineer in APL's Electro-Optical Systems Group since joining APL in June 1994. Currently working on midwave measurements of marine environments, she has also contributed to the analysis of image processing algorithms for an infrared seeker. She is an active member of the Baltimore–Washington Section of the Society of Women Engineers. Her e-mail address is Emily.Claussen@jhuapl.edu.